

Controlling Crystal Morphology of Anisotropic Zeolites with Elemental Composition

Ondřej Veselý,* Mariya Shamzhy, Wiesław J. Roth, Russell E. Morris, and Jiří Čejka



Cite This: <https://doi.org/10.1021/acs.cgd.3c01312>



Read Online

ACCESS |



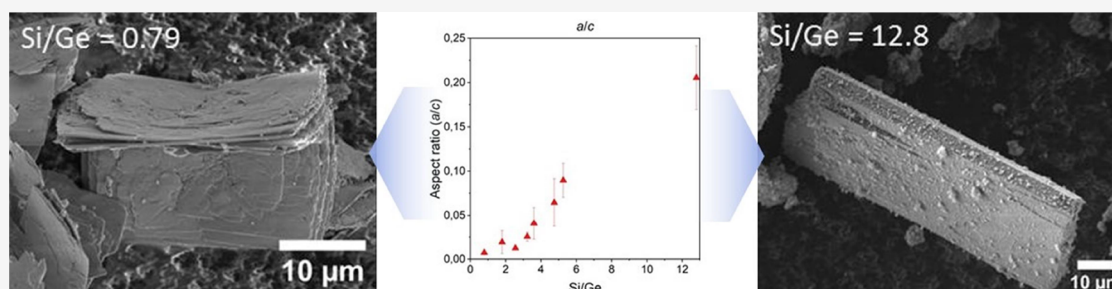
Metrics & More



Article Recommendations



Supporting Information



ABSTRACT: The morphology of zeolite crystals strongly affects their textural, catalytic, and mechanical attributes. However, controlling zeolite crystal morphology without using modifiers or structure-directing agents remains a challenging task because of our limited understanding of the relationships between zeolite crystal shape, crystallization mechanism, and composition of the starting synthesis mixture. In this study, we aimed at developing a general method for controlling the morphology of zeolites by assessing the impact of the Si/T molar ratio of the synthesis gel on the growth rate of zeolite crystals in various crystallographic directions and on the final crystal morphology of the UTL germanosilicate with a 2D system of intersecting 14- and 12-ring pores. Our results showed that flat UTL crystals progressively thicken with the Si/Ge molar ratio, demonstrating that Ge concentration controls the relative rate of crystal growth in the perpendicular direction to the pore system. The morphology of other zeolites and zeotypes with an anisotropic structure, including AFI (12R), IFR (12R), MWW (10–10R), and IWW (12–10–8R), can also be predicted based on their Si/T ratio, suggesting a systematic pattern across zeolite structures and in a wide range of zeolite framework elements. Combined, these findings introduce a facile and cost-efficient method for directly controlling crystal morphology of zeolites with anisotropic structures with a high potential for scale-up while providing further insights into the role of elemental composition in zeolite crystal growth.

INTRODUCTION

Silicate and aluminosilicate zeolites stand out for their role in numerous industrial processes involving adsorption, gas separation, and shape-selective acid catalysis.^{1–9} Related frameworks based on aluminophosphates and including isomorphous substitution with Ti, Fe, and other elements are also applied in the industry.¹⁰ Zeolites are microporous crystalline materials with frameworks consisting of corner-sharing, four-connected TO₄ (T = Si, Al, Ge, and Fe, among others) tetrahedra.^{11,12} They have a wide range of applications thanks to their thermal stability, safe handling, and activity versatility/tuneability through changes in structure, porosity, and composition. Their textural (e.g., pore size, pore accessibility, and surface area), acid (e.g., acid strength and concentration of acid sites), and physical (e.g., particle size and mechanical strength) properties, in particular, vary with structure, elemental composition, and crystal size and morphology.^{8,13–17}

The morphology of zeolites can be adjusted using growth modifiers or specially designed structure-directing agents

(SDAs).^{18–23} However, these agents significantly increase synthesis costs and hinder potential large-scale applications, even though the main criterion is usually clear-cut performance benefits. Moreover, industrial production demands a simple and general method for controlling zeolite morphology by altering fundamental synthesis conditions (e.g., temperature, stirring, water content, or elemental composition of the synthesis gel).²⁴

Synthesis conditions can be changed to control zeolite crystal growth and morphology, as previously illustrated with LTL or FAU zeolites.^{22,25–27} However, this approach is only valid for specific morphologies, lacking general principles applicable to a wide set of zeolite frameworks. The difficulty in setting guidelines derives from our limited understanding of zeolite

Received: November 6, 2023

Revised: February 28, 2024

Accepted: February 28, 2024

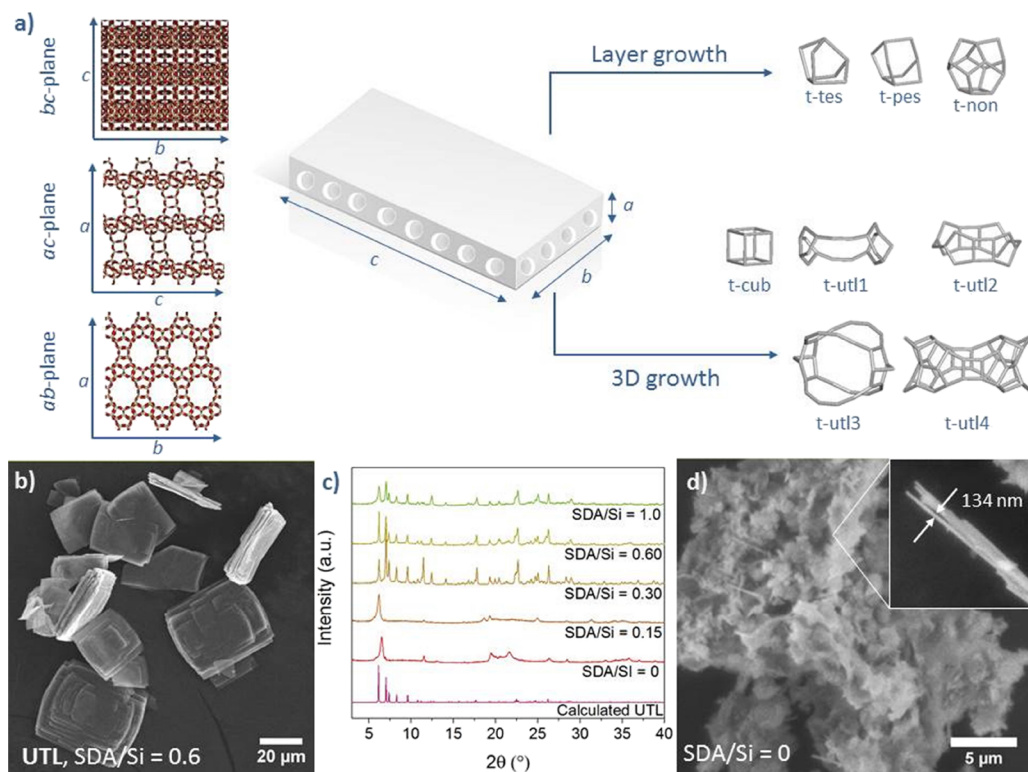


Figure 1. (a) Schematic representation of a UTL zeolite crystal with projections along the *a*-, *b*-, and *c*-axes and building units involved in layer and 3D growth; (b) SEM image of UTL (Si/Ge = 3.22; SDA/Si = 0.6); (c) powder XRD patterns of UTL synthesized with various SDA/Si ratios; and (d) SEM image of a material prepared under SDA/Si = 0.

growth mechanisms and from the lack of clear-cut relationships between synthesis conditions (e.g., gel composition), crystallization rate, and final crystal morphology.

Zeolite crystal morphology arises from the equilibrium between crystal growth rates in all crystallographic directions as equal relative crystal growth rates produce highly symmetric crystals (e.g., cubes, octahedra), while markedly different rates result in less isotropic crystal shapes.²⁸ In this context, the condensation of silicate species from the synthesis gel into a complete cage or a building unit with as few uncondensed silanol groups as possible has been proposed as the rate-determining step of zeolite crystal growth.²⁹ Despite extensively describing zeolite growth mechanisms on pure silica zeolite models and validating their conclusions by comparing predicted crystal morphologies to experimentally prepared zeolite crystals, these modeling studies overlooked the effects of synthesis conditions, such as elemental composition, choice of SDA, temperature, and water content, on zeolite crystal morphology due to the computational requirements of such modeling.^{30,31} For these reasons, controlling the crystal morphology of zeolites remains a challenging task.

In this study, we aimed at developing a method for controlling the morphology of zeolites by assessing the effect of heteroelement (i.e., nonsilicon) framework atoms on the crystal morphology of a wide range of zeolites with varying topologies and elemental composition. For our experiments, we chose germanosilicate zeolites UTL (14–12R) and IWW (12–10–8R). UTL forms flat rectangular crystals with a two-dimensional channel system running parallel to the largest plane. Accordingly, we hypothesized that the anisotropy of its pore system or the uneven size of the building units would affect crystal growth rates along different crystallographic axes and that

the growth rate along the *a*-axis should vary with the Si/Ge ratio, given the presence of Ge-rich D4R units in this direction. IWW germanosilicate contains a three-dimensional channel system composed of 12–10- and 8-rings and is thus suitable for determining whether the morphology evolution originates from the position of the Ge-rich D4Rs, the direction of the pores, or the size of the building units. By scanning electron microscopy (SEM), we examined the crystal morphology of UTL and IWW germanosilicates and their variation as a function of the Si/Ge molar ratio. Our findings provide a general and efficient approach to controlling zeolite crystal morphology by changing the Si/T ratio of the synthesis gel.

RESULTS

UTL Zeolite. The initial experiments were performed with UTL germanosilicate (IM-12,³² ITQ-15³³) for its structural features. More specifically, the UTL topology contains intersecting 14R and 12R channels arranged into a 2D pore system. These channels are sandwiched between parallel nonporous *pcr*¹ layers connected by cubical D4R units into the three-dimensional UTL framework (see Figure 1a).³² Furthermore, UTL zeolite often crystallizes as a germanosilicate with germanium atoms preferentially located in D4R units, while the layers are primarily composed of silicon as T atoms.^{35–37} As such, the UTL zeolite should provide us with a convenient tool for studying the variation of morphology as a function of synthesis conditions.

UTL crystals resemble thin flat platelets with dimensions ranging from 0.5 to 1.0 μm along the *a*-axis (thickness) and from 10 to 50 μm in *b*- and *c*-axes, as reported in previous studies.^{32,38–40} However, whether the crystal size strongly depends on synthesis conditions remains unclear. For this

reason, we minimized sources of variability by using the same equipment (20 mL Teflon-lined steel autoclaves and rotary oven), settings (rotation speed, and heating rate, among other parameters), and conditions (synthesis temperature and time) in our experiments. We also ensured that each synthesis was carried out under the same initial pH by adjusting its value to pH = 10.5 prior to the hydrothermal treatment.

Under these synthesis conditions, we prepared UTL zeolite with a framework Si/Ge molar ratio of 3.22 and crystals with an average size of $43.7 \times 32.5 \times 0.84 \mu\text{m}^3$ (Figure 1b). The crystals consisted of flat rectangular lamellae stacked and intergrown into larger crystals. The crystal lamellae were rectangular, with 90, 90, and 105.1° angles between the facets, matching the angles of the UTL unit cell and, thus, enabling us to easily identify the crystallographic axes. The crystallographic axes were assigned for each subsequent sample individually (Figure S1 illustrates the axis assignment on UTL with Si/Ge = 5.26). This flat crystal morphology derives from differences in the relative rate of crystal growth caused by the structural features of the UTL framework (vide supra).²⁸

For clarity, we analyzed layer growth (*b*- and *c*-axis) and growth in the third dimension (*a*-axis) separately. UTL zeolite layers are propagated through the formation of small *t*-tes, *t*-pes, and *t*-non cages. In contrast, the growth along the *a*-axis involves not only the rapid formation of D4R (*t*-cub) units but also the slow formation of large cages at the channel intersections (i.e., *t*-utl-1, *t*-utl-2, *t*-utl-3, or *t*-utl-4). As a result, layer propagation is faster than growth in the third dimension, thereby explaining the flat, wide crystals.

Alternatively, we may interpret the large cages as a byproduct of the subsequent formation of *t*-cub, *t*-non, and *t*-tes or *t*-pes cages into an “arch”, which corresponds to the *pcr* layer. However, even from this point of view, the *a*-axis growth requires multiple steps, involving a large number of less stable and partly condensed Si species. The formation of these large cages also requires stabilization by SDA molecules, as shown by repeating the UTL synthesis with a lower SDA concentration in the synthesis mixture. Synthesis with SDA/Si ≥ 0.3 yielded a fully crystalline UTL zeolite (Figure 1c), while synthesis with SDA/Si ≤ 0.15 yielded only a partly ordered lamellar material with 134 nm-thick sheets (Figure 1d). The results confirm that an SDA content above SDA/Si = 0.3 is crucial for stabilizing the large cavities and forming the UTL framework.

We tested our first hypothesis by synthesizing a series of UTL zeolites with Si/Ge ratios ranging from 0.79 to 12.8. The synthesis mixtures possessed the same pH as well as SDA/Si molar ratios. We did not consider changes in local SDA concentration or in the strength of SDA-framework interactions since the synthesis differed only in the ratio of Si and Ge, which both possess the same charge. The synthesis yielded zeolites with UTL structure as verified by the X-ray powder diffraction (XRD) (Figure 2a). We calculated the crystallite size along *a*-, *b*-, and *c*-axes from the full width at half-maximum (fwhm) of 200, 020, and 001 diffraction peaks at $2\theta = 6.12$, 12.64 , and 7.36° , respectively. The overall crystallite size increased with increasing Si/Ge ratio. The lower germanium content decelerated the nucleation resulting in longer crystallization time and the formation of larger crystals. Additionally, the *h*/*l* and *k*/*l* aspect ratios of the crystallites also increased with Si/Ge implying that the crystallite shape also changes with Si/Ge (Figure 2b). Particularly, the crystallites became thicker and wider along the *a*- and *b*-axes with increasing content of Si. It is important to note that the crystallite size is not interchangeable with the bulk

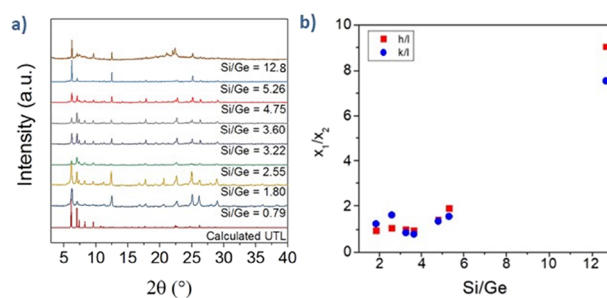


Figure 2. (a) Powder XRD patterns of UTL samples; (b) variation of the *h*/*l* and *k*/*l* aspect ratios of the crystallites.

crystal morphology of the UTL (as the bulk crystallites can consist of a large number of small crystallite domains) and does not have to follow the same trends.

Hence, we analyzed the bulk morphology of the UTL crystals by SEM imaging. The SEM images showed that the UTL with Si/Ge = 0.79 consisted of thin rectangular crystals, averaging 30, 23, and $0.16 \mu\text{m}$ along the *c*-, *b*- and *a*-axis, respectively (Figure 3). The average size was calculated from images of at least five separate crystals.

Increasing the Si/Ge ratio from 0.79 to 12.8 progressively increased the average crystal size to 79, 27, and $5.4 \mu\text{m}$ along the *c*-, *b*-, and *a*-axis, respectively (Figure 4b). To assess the variation of the crystal morphology as a function of Si/Ge, we calculated

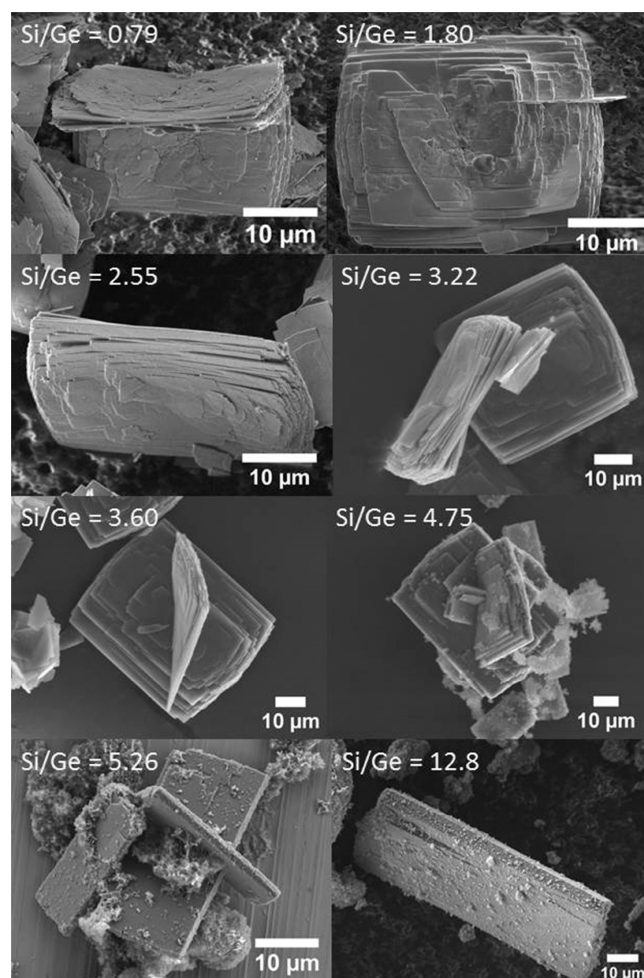


Figure 3. SEM images of UTL zeolites with varying Si/Ge molar ratios.

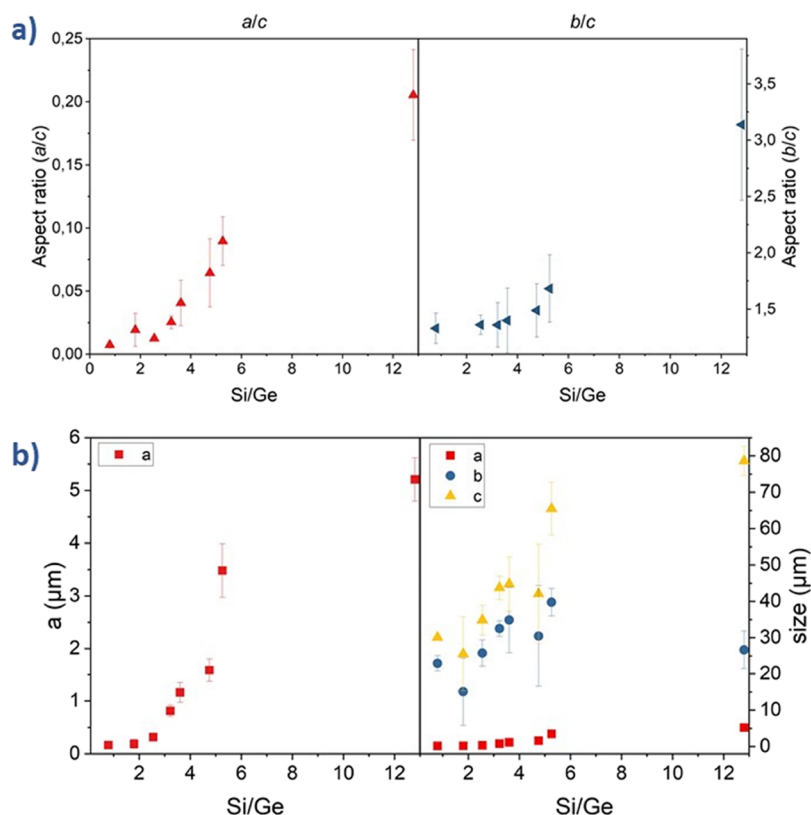


Figure 4. (a) Variation of crystal aspect ratios and (b) variation of crystal sizes along the *a*-, *b*-, and *c*-axes as a function of Si/Ge.

the crystal aspect ratios along the *b/c* and *a/c* axes. Figure 4a shows a steady increase in *b/c* and *a/c* aspect ratios with Si/Ge, highlighting that Si/Ge alone determines the crystal morphology of UTL germanosilicate. UTL crystals undergo two morphological changes. First, the *b/c* aspect ratio increases with the increase in the Si/Ge ratio (i.e., with the decrease in Ge content) because germanium is crucial for the formation of *t-cub* (D4R) units. The density of the *t-cub* units is higher along the *c*-axis. Increasing the germanium content favors the formation of these units and, as a result, the expansion of the crystal along the *c*-axis, which manifests as decreasing *b/c* aspect ratio with increasing germanium content.

UTL samples with Si/Ge ≥ 4.75 also contained particles of amorphous matter (Figure 3). This amorphous phase was also inferred from the textural properties of the samples, especially from the low volume of the micropores, more specifically 0.15 and 0.03 cm³/g, in samples with Si/Ge = 5.26 and 12.8, respectively (Table S1). The argon adsorption isotherms of these samples also deviate from the typical type I toward type II due to interparticle adsorption at higher relative pressures (Figure S2). The interparticle adsorption likely occurs between the amorphous particles in the sample. The amorphous particles originated from leftover uncrystallized synthesis gel, suggesting that the nucleation rate decreases with the increase in the Si/Ge ratio. If germanium is essential to nucleation in proportion to silicon, then silicon cannot be fully consumed in Ge-poor synthesis mixtures. Consequently, a portion of the unused silica precipitates, forming amorphous particles.











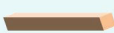







Ge-rich mixtures (samples with Si/Ge = 0.79 and 1.80) contained more germanium than UTL can accommodate. Unsurprisingly, the excess germanium precipitated as germanium oxide, thereby decreasing the micropore volume (Figure S3).⁹ The decrease in the nucleation rate with the increase in Si/

Ge led to the formation of larger crystals. These results are in line with our observations (Figure 3) and with previous findings of Shvets et al., who also noticed a similar variation in UTL zeolite crystal morphology and size as a function of the Si/Ge molar ratio.³⁹

Based on the comment of the referee, we have also considered the synthesis duration as a possible factor that may influence the UTL crystal morphology. The anisotropic nature of the UTL framework implies that the crystal growth rate varies along the individual crystallographic axes. Hence, the crystal shape and aspect ratios may, hypothetically, evolve with time. The characteristic powder XRD pattern of UTL emerged after only 3 days of synthesis time (Figure S4a). Nevertheless, sampling of the synthesis mixture in a range from 2 to 13 days revealed no clear evolution of crystal shape in time (Figure S4b). The sample recovered after 3 days contained typical flat crystals $32 \times 21 \times 0.23 \mu\text{m}^3$ in size covered in smaller amorphous particles (Figure S5). The intensity of the characteristic XRD reflections increased with synthesis time accompanied by the gradual vanishing of the amorphous matter, while the average crystal size and aspect ratio remained virtually unchanged. It is clear, that the UTL undergoes rapid crystal growth in the early stage of the synthesis (<2 days) followed by a relatively stagnant stage characterized by only minor changes in crystal size and aspect ratio.

In summary, increasing the Si/Ge ratio decelerates the nucleation and prolongs the crystallization time of the UTL germanosilicate. On the other hand, both isolated crystallites and bulk crystals of UTL exhibit increase of *a/c* and *b/c* crystal aspect ratio, meaning that the crystal morphology also changes. The germanium atoms promote the nucleation but at the same time impede the crystal growth along the *a*- and partially along the *b*-axis.

Table 1. List of Zeolite Structures Whose Crystal Morphology Varies as a Function of the Si/T Ratio

Structure type (IZA)	Material	Pore system	Elements	Morphology		Ref.
*MRE	ZSM-48	10R	Si, Al			[44]
AFI	SAPO-5	12R	Si, Al, P			[43]
IFR	ITQ-4	12R	Si, Al			[41]
LTL	Zeolite L	12R	Si, Al			[22]
MWW	MCM-22P, MCM-56	10-10R	Si, Al			[45-47]
TUN	TNU-9	10-8R	Si, Al			[48]
MOR	Mordenite	12-8R	Si, Al			[49]
UTL	IM-12	14-12R	Si, Ge			This study
IWW	ITQ-22	12-10-8R	Si, Ge			This study

Extension to Other Frameworks. Similar response to the Si/Al ratio has been observed for the **MWW** zeolite. The **MWW** is an aluminosilicate zeolite with a two-dimensional 10–10R channel system. **MWW** aluminosilicate crystallizes as a semi-ordered layered precursor MCM-22P, as monolayered (disordered) MCM-56 or as 3D MCM-49.^{46,50} MCM-22P is formed by decreasing the aluminum content in the synthesis gel so that the layers are aligned into a semiordered structure through H-bonding but lack covalent interlayer connections. In contrast, preparing a fully connected three-dimensional MCM-49 framework requires a high aluminum content and involves the formation of a unilamellar intermediate MCM-56 consisting of disordered single layers. Under specific conditions, MCM-56 is the final product.^{45,47} Yet, despite its structural specificities, **MWW** zeolites are formed following patterns similar to those discussed above. The aluminum in the synthesis mixture, on the one hand, facilitates the formation of interlayer connections and a condensed 3D framework, but on the other hand, decelerates crystal growth in the interlayer direction. Additionally, the entire gel converts first to unilamellar MCM-56 and only after to MCM-49 (3D form) under moderately alkaline conditions.⁵¹ The reduced growth rate of **MWW** results in thinner crystals along the interlayer axis. In the presence of aniline and under high H₂O/Si ratio, crystal thickness decreases to that of a single unit cell, yielding isolated MCM-56 layers.^{46,47}

Crystal morphology is also correlated to elemental composition in other zeolites, as outlined in Table 1. For example, increasing the Si/Al molar ratio (i.e., the silicon content) of **LTL**, with unidimensional 12R pores, promotes growth perpendicularly to the pores, increasing the width and simultaneously decreasing the length of the crystals, which consist of hexagonal rods elongated in the direction of the 12R pores.²² Similarly, in **IFR** zeolite, which also contains unidimen-

sional 12R channels, decreasing the content of aluminum from 1.52 Al per unit cell to 0.44 Al per unit cell (i.e., increasing the Si/Al ratio) produces thicker prismatic crystals elongated along the direction of the pores.⁴¹ Decreasing the aluminum content in **MTW** zeolite from Si/Al ratio 35 to 120 also increases the zeolite crystal size by slowing nucleation; however, without significantly affecting the crystal morphology. The morphology change may not have occurred due to the relatively low aluminum content in the respective samples.⁴² In this study, the Si/Ge effect on **UTL** crystal morphology weakened when increasing Si/Ge concentrations to 5.26 and 12.8 (Figure 3b). Moreover, increasing the Si/Ge ratio to 12.8 decreased the overall crystallinity (Figure 3a), promoting the formation of amorphous unused silica (vide infra). Unfortunately, we were unable to synthesize **UTL** at higher Si/Ge concentrations (data not shown). Therefore, we could not verify whether the effect is exclusive for low Si/T ratios, and the morphology of **UTL** remains unaffected at Si/Ge between 35 and 120.

Silico-aluminophosphate SAPO-5 (**AFI**, 12R) undergoes a similar change in morphology transition as a function of its Si content because increasing the Si content produces thicker crystals perpendicularly to the channel system.⁴³ This example suggests that the correlation between crystal morphology and Si/T ratio may be valid for a wide range of porous materials beyond zeolites.

Overall, our results with **UTL** zeolite corroborate the findings of studies with other zeolites, summarized in Table 1, which consistently report the correlation between zeolite crystal morphology and its Si/T molar ratio. By extrapolation, we propose that the crystal morphology of zeolites (and possibly other porous solids) with a one- or two-dimensional pore system predictably varies with the Si/T ratio. Increasing the Si content of a framework promotes crystal growth in the crystallographic

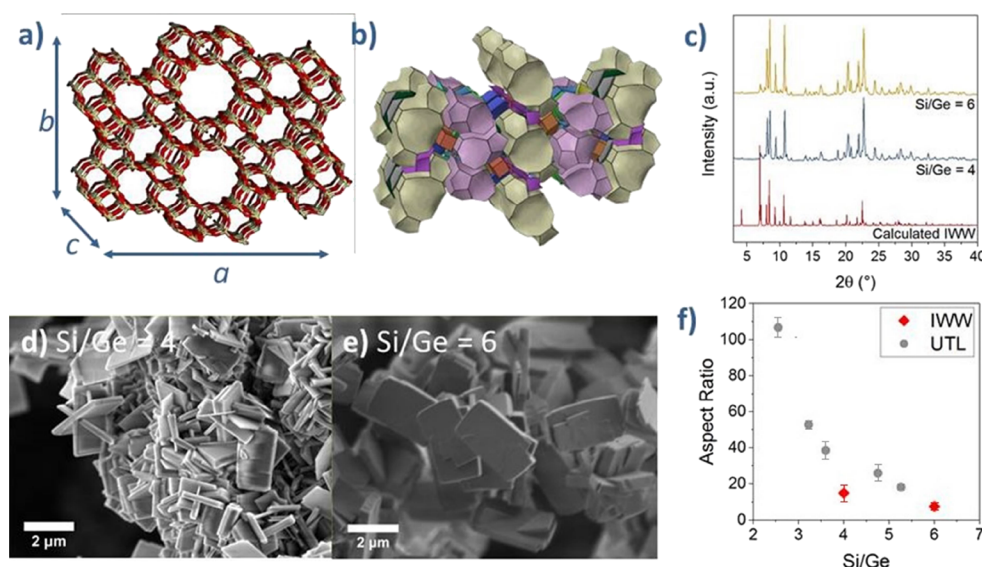


Figure 5. (a) Schematic representation of the IWW structure; (b) arrangement of the building units in the IWW structure; (c) powder XRD patterns of the IWW samples; (d) SEM image of IWW (Si/Ge = 4); (e) SEM image of IWW (Si/Ge = 6); and (f) variation of the IWW and UTL crystal aspect ratios as a function of the Si/Ge.

dimension perpendicular to the direction of the pores, resulting in thicker crystals in the respective direction(s).

IWW. As shown above and in previous studies,^{22,43–49} increasing Si/T enhances crystal growth in directions perpendicular to the pores in a wide range of zeolites with one- or two-dimensional channel systems with significant structural anisotropy. Such framework anisotropy should also be observed in anisotropic zeolites with 3D channel systems of unevenly large pores. To test this assumption, we selected IWW (ITQ-22) germanosilicate as a model zeolite.⁵²

Because the IWW structure contains a three-dimensional system of interconnected 12-, 10-, and 8R pores (Figure 5a), IWW crystals should be elongated in the directions of the *c*-axis parallel to the largest 12R pores. Considering the arrangement of the large building units into a row along the *b*-axis (Figure 5b), we further hypothesized that the IWW crystal is longer along the *b*-axis than along the *a*-axis and grows more along the *b*- and *a*-axes, perpendicular to the 12R channels, when increasing the Si/Ge ratio.

The powder XRD patterns of our IWW zeolite samples with Si/Ge = 4 and 6 showed reflections typical of the IWW framework (Figure 5c). Nevertheless, we observed differences in their relative intensities, which might have resulted from the preferred crystal orientation, suggesting differences in the crystal morphology between samples. For this reason, we analyzed the crystal morphology of the IWW samples by SEM.

SEM imaging of IWW germanosilicate with Si/Ge = 4 revealed agglomerates and intergrowths of flat rectangular crystals averaging $2.36 \mu\text{m} \times 1.34 \mu\text{m} \times 0.16 \mu\text{m}$ (Figure 5d,e). In turn, transmission electron microscopy (TEM) imaging of the IWW sample with Si/Ge = 4 enabled us to identify the crystallographic axes in the IWW zeolite crystals (Figure S6). At high magnification, we confirmed that the projection of the crystal lattice matches the *a,b*-plane of the IWW topology. We also verified the crystal *a,b*-facet by comparing our SEM images to those of a previously published HR-TEM study of IWW.⁵³ Based on the “broken” *a*-edge, which gives the *a,b*-facet its distinguished semihexagonal shape, we identified the crystallographic directions. The crystal sizes were $a = 0.16 \mu\text{m}$, $b = 2.36$

μm , and $c = 1.34 \mu\text{m}$, in line with our estimates; the crystals were elongated along the *c*-axis, while the array of 12R pores decelerated the growth along the *a*-axis, thus reducing crystal size in the *a*-axis. The reason for the unexpectedly pronounced *b*-axis growth remains elusive.

Upon increasing the Si/Ge ratio from 4 to 6, the size of the IWW crystals increased from $0.16 \times 2.36 \times 1.34$ to $0.38 \times 2.79 \times 1.50 \mu\text{m}$ (Figure 5e). IWW showed the most pronounced growth along the *a*-axis, which lies perpendicular to the array of the 12R pores. The aspect ratio of the IWW zeolite followed the trend observed in UTL (Figure 4f), thereby validating our hypothesis that the morphology of anisotropic zeolites varies with their Si/T ratio whether they have one-, two-, or three-dimensional channel systems.

CONCLUSIONS

The crystal morphology of the UTL germanosilicate zeolite predictably varies with the Si/Ge molar ratio. The Si/Ge ratio determines the aspect ratio of the crystallographic *b*- and *c*-axes parallel to the two-dimensional pore system of UTL against the perpendicular *a*-axis. This uneven crystal shape reflects differences in crystal growth rates along different axes caused by the uneven arrangement of the building units. In other aluminosilicate and germanosilicate zeolites with anisotropic structural features (e.g., one- or two-dimensional pore system), including MWW, MOR, *MRE, or LTL, increasing the Si/T ratio also promotes crystal growth in direction(s) perpendicular to the pore system or arrays of large building units. Therefore, zeolite crystal morphology can be predicted and controlled based on the Si/T ratio, and this approach is valid for a wide range of zeolites with varying structure topologies and compositions. Because crystal morphology is crucial for tuning the textural and mechanical properties of zeolite-based materials, this approach may be a simple and reliable scale-up method.

EXPERIMENTAL METHODS

Synthesis of SDAs. UTL germanosilicates were synthesized using 2,6-dimethyl-5-azoniaspiro[4.5]decane (DMASD) bromide as a

SDA.³⁹ DMASD was prepared by mixing 60 mL of 1,4-dibromobutane, 82.9 g of K₂CO₃, and 500 mL of acetonitrile in a round-bottom flask. In addition, 67 mL of 2,6-dimethylpiperidine was added to the mixture. The reaction was performed at 85 °C, refluxing for 24 h. Subsequently, the acetonitrile was evaporated. The solid product was dissolved in ethanol, and the insoluble K₂CO₃ was removed by filtration. The ethanol solution was concentrated by evaporation; DMASD was precipitated by the addition of diethyl ether and recovered by filtration. The structure of DMASD was verified by ¹H NMR spectroscopy. This SDA was ion exchanged for the hydroxide form using Ambersep 900(OH) ion-exchange resin with a 2:1 SDA:resin w/w ratio.

IWW germanosilicates were synthesized using 1,5-bis-(methylpyrrolidinium)pentane dihydroxide (MPP).⁵² MPP was prepared by mixing 18.8 g of 1,5-dibromopentane and 20 g of N-methylpyrrolidine in 150 mL of acetone and refluxed for 20 h. The product was collected by filtration, washed with acetone, and dried under vacuum overnight. The structure of the SDA was verified by ¹H NMR spectroscopy, using deuterium oxide as a solvent. MPP was ion exchanged for hydroxide form using anionic exchange resin (OH type of Ambersep 900) (8 mmol of SDA/g resin). Subsequently, the excess water in the SDA solution was evaporated at 35 Torr and 35 °C to a hydroxide concentration of 1.0 M.

UTL Synthesis. The germanosilicate UTL zeolite was prepared by dissolving germanium oxide in a 0.6 M solution (unless stated otherwise) of DMASD hydroxide. Once the germanium oxide was fully dissolved, fumed silica (Cab-O-Sil) was added to the mixture and stirred until dissolved. The final molar composition of the synthesis mixture was $x\text{SiO}_2:1 - x\text{GeO}_2:0.4\text{ SDA}:33.3\text{H}_2\text{O}$, where x represents the Si/(Si + Ge) molar ratio. The pH of the synthesis gel was adjusted to 10.5 by the addition of DMASD hydroxide or diluted (0.01 M) HCl solution. Diluted 0.01 M solution of LiOH was used to adjust the pH of UTL synthesis with reduced SDA/Si molar ratios. The synthesis mixture was transferred to 20 mL Teflon-lined stainless-steel autoclaves. Crystallization was performed at 175 °C for 8 days with agitation (200 rpm). The resulting product was recovered by filtration, washed with water, and dried at 60 °C. The products were calcined at 550 °C for 6 h in airflow to remove the organic template.

IWW Synthesis. The germanosilicate IWW samples were prepared by dissolving the required amounts of germanium dioxide (Sigma-Aldrich, 99.99%) and tetraethyl orthosilicate (Sigma-Aldrich, 98%) in MPP solution. The ethanol formed by hydrolysis of tetraethylorthosilicate was evaporated under stirring. The final mixture with molar composition $x\text{SiO}_2:1 - x\text{GeO}_2:0.25\text{ MPP}:15\text{H}_2\text{O}$ was transferred to Teflon-lined stainless-steel autoclaves and heated to 175 °C K for 11 days. The final products were recovered by centrifugation, washed with water, and dried at 60 °C overnight. The resulting solids were calcined at 580 °C for 6 h in air.

Characterization Methods. The crystallinity and crystal structure of the samples were analyzed by XRD on a Bruker D8 Advance diffractometer equipped with a Linxeye XE-T detector in the Bragg–Brentano geometry using Cu K α ($\lambda = 0.15406$ nm) radiation. Data were collected over the 2θ range of 3–40° with a 0.021° step size at 0.8 s per step. Crystallite size, L , in $h00$, $0k0$, and $00l$ directions was calculated using the Scherrer equation:

$$L_{hkl} = \frac{K \cdot \lambda}{\beta \cdot \cos\theta}$$

where K represents the shape factor fixed at 0.89, λ is the wavelength of the X-ray source, β is the fwhm of the respective diffraction peak, and θ is its diffraction angle.

Crystal size and morphology were examined by SEM imaging under a JEOL IT-200 microscope in secondary electron imaging mode at an electron beam accelerating voltage of 15 kV and a working distance of 10 mm. Additional measurements were performed using a JEOL IT-800 microscope in secondary electron imaging mode at an electron beam accelerating voltage of 3 kV and a working distance of 2 mm. Aspect ratios of the crystals were calculated as x_1 divided by x_2 , where x_1 and x_2 represent two of the crystallographic axes. The presented aspect

ratio values were calculated as an arithmetic average of values obtained from at least five different crystals:

$$\text{AR}(x_1/x_2) = \frac{x_1}{x_2}$$

The Ge content and Si/Ge ratio of zeolites were determined by inductively coupled plasma mass spectrometry (ICP-MS) analysis (Agilent 7900 ICP-MS; Agilent Technologies, Inc., USA). Approximately 50 mg of the sample was mixed with 1.8 mL of HNO₃ (67–69%, ANALPURE), 5.4 mL of HCl (34–37%, ANALPURE), 1.8 mL of HF (47–51%, ANALPURE), and then transferred into a closed Teflon vessel, placed in the microwave (Speedwave XPERT, Berghof) and heated at 210 °C (5 °C/min) for 25 min. After cooling, the complexation of the surplus HF was performed by adding 12 mL of H₃BO₃, followed by microwave treatment at 190 °C (5 °C/min) for 10 min. Once cooled down, the solutions were diluted for analysis.

TEM imaging was performed using a JEOL NeoARM 200 F microscope equipped with a Schottky-type field emission gun operated at an accelerating voltage of 200 kV. The microscope was aligned using a gold nanoparticle sample as the standard to reach atomic resolution.

Argon adsorption–desorption isotherms were obtained on a Micromeritics 3Flex volumetric Surface Area Analyzer at –186 °C in liquid argon bath. The samples were degassed on a Micromeritics Smart Vac Prep instrument under vacuum at 250 °C for 8 h with heating rate 1 °C min^{–1} under vacuum (3×10^{-2} mmHg minimum pressure). The specific surface area was calculated using the Brunauer–Emmett–Teller method in the relative pressure range from $p/p_0 = 0.05$ to $p/p_0 = 0.25$. The micropore volume (V_{mic}) was calculated by using the t -plot method. The total pore volume (V_{tot}) was calculated from the adsorbed amount at a relative pressure of $p/p_0 = 0.98$.

■ ASSOCIATED CONTENT

SI Supporting Information

The Supporting Information is available free of charge at <https://pubs.acs.org/doi/10.1021/acs.cgd.3c01312>.

SEM images of UTL zeolite crystal with spatial a -, b -, and c -axes; argon adsorption–desorption isotherms, and textural properties of UTL samples; correlation of the Si/Ge molar ratios in the synthesis gel and in solid and sample pore volumes; and powder XRD patterns and SEM images of UTL samples with varying synthesis time (PDF)

■ AUTHOR INFORMATION

Corresponding Author

Ondřej Veselý – Faculty of Sciences, Charles University, 128 43 Prague 2, Czech Republic; orcid.org/0000-0002-8350-7725; Email: ondrej.vesely@natur.cuni.cz

Authors

Mariya Shamzhy – Faculty of Sciences, Charles University, 128 43 Prague 2, Czech Republic; orcid.org/0000-0002-1979-6817

Wiesław J. Roth – Faculty of Chemistry, Jagiellonian University, 30-387 Krakow, Poland; orcid.org/0000-0002-4090-8043

Russell E. Morris – EaStChem School of Chemistry, University of St. Andrews, St. Andrews KY16 9ST, U.K.; orcid.org/0000-0001-7809-0315

Jiří Čejka – Faculty of Sciences, Charles University, 128 43 Prague 2, Czech Republic; orcid.org/0000-0003-1400-1031

Complete contact information is available at: <https://pubs.acs.org/10.1021/acs.cgd.3c01312>

Notes

The authors declare no competing financial interest.

ACKNOWLEDGMENTS

O.V. acknowledges the support of Charles University through the project “Grant Schemes at CU” (Reg. no. CZ.02.2.69/0.0/0.0/19_073/0016935). J.Č. acknowledges the support of the Czech Science Foundation through the project ExPro (19-27551X). W.J.R. acknowledges the financial support from the National Science Centre Poland, grant number 2020/37/B/ST5/01258. M.S. acknowledges the support of the Ministry of Education, Youth and Sports of the Czech Republic through ERC_CZ project LL 2104. This work was also supported by Ministerstvo Školství, Mládeže a Tělovýchovy as ERDF/ESF project TECHSCALE (Nos. CZ.02.01.01/00/22_008/0004587). The authors thank Emad Shamma for supplementary SEM measurements and Carlos V. Melo for editing the manuscript. R.E.M. acknowledges the European Research Council for funding through the AdG 787073 “ADOR” programme.

ADDITIONAL NOTE

¹In this study, we adopted the lowercase, 3-letter designation of layers according to Gies and Marler³⁴ Marler, B.; Gies, H. Hydrous layer silicates as precursors for zeolites obtained through topotactic condensation: a review, *Eur. J. Mineral.* **2012**, *24*, 405–428.

REFERENCES

- Čejka, J.; Morris, E.R.; Nachtigall, P. *Zeolites in Catalysis: Properties and Applications*; The Royal Society of Chemistry, 2017.
- Vogt, E.T.C.; Whiting, G.T.; Chowdhury, A. D.; Weckhuysen, B.M., Chapter Two - Zeolites and Zeotypes for Oil and Gas Conversion, in: Jentoft, F.C. (Ed.) *Adv. Catal.*; Academic Press, 2015; 143–314.
- Moliner, M.; Martínez, C.; Corma, A. Multipore Zeolites: Synthesis and Catalytic Applications. *Angew. Chem., Int. Ed.* **2015**, *54*, 3560–3579.
- Li, Y.; Li, L.; Yu, J. Applications of Zeolites in Sustainable Chemistry. *Chem.* **2017**, *3*, 928–949.
- Blauwhoff, P.M.M.; Gosselink, J.W.; Kieffer, E.P.; Sie, S.T.; Stork, W.H.J., Zeolites as Catalysts in Industrial Processes, in: Weitkamp, J.; Puppe, L. (Eds.) *Catalysis and Zeolites: Fundamentals and Applications*; Springer Berlin Heidelberg: Berlin, Heidelberg, 1999; 437–538.
- Pina, M. P.; Mallada, R.; Arruebo, M.; Urbiztondo, M.; Navascues, N.; de la Iglesia, O.; Santamaria, J. Zeolite films and membranes, Emerging applications. *Microporous Mesoporous Mater.* **2011**, *144*, 19–27.
- Park, K. H.; Park, H. J.; Kim, J.; Ryoo, R.; Jeon, J. K.; Park, J.; Park, Y. K. Application of Hierarchical MFI Zeolite for the Catalytic Pyrolysis of Japanese Larch. *J. Nanosci. Nanotechnol.* **2010**, *10*, 355–359.
- Martinez, C.; Corma, A. Inorganic molecular sieves: Preparation, modification and industrial application in catalytic processes. *Coord. Chem. Rev.* **2011**, *255*, 1558–1580.
- Čejka, J.; Centi, G.; Perez-Pariente, J.; Roth, W. J. Zeolite-based materials for novel catalytic applications: Opportunities, perspectives and open problems. *Catal. Today* **2012**, *179*, 2–15.
- Fechete, I.; Wang, Y.; Védrine, J. C. The past, present and future of heterogeneous catalysis. *Catal. Today* **2012**, *189*, 2–27.
- Maesen, T., The Zeolite Scene – An Overview, in: Čejka, J.; van Bekkum, H.; Corma, A.; Schüth, F. (Eds.) *Stud. Surf. Sci. Catal.*; Elsevier, 2007; 1–12.
- McCusker, L.B.; Baerlocher, C., Zeolite Structures, in: Čejka, J.; van Bekkum, H.; Corma, A.; Schüth, F. (Eds.) *Stud. Surf. Sci. Catal.*; Elsevier, 2007; 13–37.
- Shamzhy, M.; Opanasenko, M.; Concepción, P.; Martínez, A. New trends in tailoring active sites in zeolite-based catalysts. *Chem. Soc. Rev.* **2019**, *48*, 1095–1149.
- Kubu°, M.; Žilková, N.; Čejka, J. Post-synthesis modification of TUN zeolite: Textural, acidic and catalytic properties. *Catal. Today* **2011**, *168*, 63–70.
- Kubu°, M.; Opanasenko, M.; Shamzy, M. Modification of textural and acidic properties of -SVR zeolite by desilication. *Catal. Today* **2014**, *227*, 26–32.
- Gil, B.; Mokrzycki, Ł.; Sulikowski, B.; Olejniczak, Z.; Walas, S. Desilication of ZSM-5 and ZSM-12 zeolites: Impact on textural, acidic and catalytic properties. *Catal. Today* **2010**, *152*, 24–32.
- del Campo, P.; Beato, P.; Rey, F.; Navarro, M. T.; Olsbye, U.; Lillerud, K. P.; Svelle, S. Influence of post-synthetic modifications on the composition, acidity and textural properties of ZSM-22 zeolite. *Catal. Today* **2018**, *299*, 120–134.
- Lupulescu, A. I.; Kumar, M.; Rimer, J. D. A Facile Strategy To Design Zeolite L Crystals with Tunable Morphology and Surface Architecture. *J. Am. Chem. Soc.* **2013**, *135*, 6608–6617.
- Na, K.; Jo, C.; Kim, J.; Cho, K.; Jung, J.; Seo, Y.; Messinger, R. J.; Chmelka, B. F.; Ryoo, R. Directing Zeolite Structures into Hierarchically Nanoporous Architectures. *Science* **2011**, *333*, 328–332.
- Kim, W.; Kim, J.-C.; Kim, J.; Seo, Y.; Ryoo, R. External Surface Catalytic Sites of Surfactant-Tailored Nanomorphous Zeolites for Benzene Isopropylation to Cumene. *ACS Catal.* **2013**, *3*, 192–195.
- Bonilla, G.; Díaz, I.; Tsapatsis, M.; Jeong, H.-K.; Lee, Y.; Vlachos, D. G. Zeolite (MFI) Crystal Morphology Control Using Organic Structure-Directing Agents. *Chem. Mater.* **2004**, *16*, 5697–5705.
- Lee, Y.-J.; Lee, J. S.; Yoon, K. B. Synthesis of long zeolite-L crystals with flat facets. *Microporous Mesoporous Mater.* **2005**, *80*, 237–246.
- Li, S.; Li, J.; Dong, M.; Fan, S.; Zhao, T.; Wang, J.; Fan, W. Strategies to control zeolite particle morphology. *Chem. Soc. Rev.* **2019**, *48*, 885–907.
- Meng, X.; Xiao, F.-S. Green Routes for Synthesis of Zeolites. *Chem. Rev.* **2014**, *114*, 1521–1543.
- Gomez, A. G.; Silveira, G. D.; Doan, H.; Cheng, C.-H. A facile method to tune zeolite L crystals with low aspect ratio. *Chem. Commun.* **2011**, *47*, 5876–5878.
- Larlus, O.; Valtchev, V. P. Crystal Morphology Control of LTL-Type Zeolite Crystals. *Chem. Mater.* **2004**, *16*, 3381–3389.
- Reiprich, B.; Weissenberger, T.; Schwiager, W.; Inayat, A. Layer-like FAU-type zeolites: A comparative view on different preparation routes. *Frontiers of Chemical Science and Engineering* **2020**, *14*, 127–142.
- Hill, A. R.; Cubillas, P.; Gebbie-Rayet, J. T.; Trueman, M.; de Bruyn, N.; Harthi, Z. A.; Pooley, R. J. S.; Attfield, M. P.; Blatov, V. A.; Proserpio, D. M.; Gale, J. D.; Akporiaye, D.; Arstad, B.; Anderson, M. W. CrystalGrower: a generic computer program for Monte Carlo modelling of crystal growth. *Chemical Science* **2021**, *12*, 1126–1146.
- Brent, R.; Cubillas, P.; Stevens, S. M.; Jelfs, K. E.; Umemura, A.; Gebbie, J. T.; Slater, B.; Terasaki, O.; Holden, M. A.; Anderson, M. W. Unstitching the Nanoscopic Mystery of Zeolite Crystal Formation. *J. Am. Chem. Soc.* **2010**, *132*, 13858–13868.
- Anderson, M. W.; Gebbie-Rayet, J. T.; Hill, A. R.; Farida, N.; Attfield, M. P.; Cubillas, P.; Blatov, V. A.; Proserpio, D. M.; Akporiaye, D.; Arstad, B.; Gale, J. D. Predicting crystal growth via a unified kinetic three-dimensional partition model. *Nature* **2017**, *544*, 456–459.
- Brent, R.; Anderson, M. W. Fundamental Crystal Growth Mechanism in Zeolite L Revealed by Atomic Force Microscopy. *Angew. Chem., Int. Ed.* **2008**, *47*, 5327–5330.
- Pailaud, J.-L.; Harbuzaru, B.; Patarin, J.; Bats, N. Extra-Large-Pore Zeolites with Two-Dimensional Channels Formed by 14 and 12 Rings. *Science* **2004**, *304*, 990.
- Corma, A.; Díaz-Cabañas, M. J.; Rey, F.; Nicolopoulos, S.; Boulahya, K. ITQ-15: The first ultralarge pore zeolite with a bi-directional pore system formed by intersecting 14- and 12-ring channels, and its catalytic implications. *Chem. Commun.* **2004**, 1356–1357.

- (34) Marler, B.; Gies, H. Hydrous layer silicates as precursors for zeolites obtained through topotactic condensation: a review. *European Journal of Mineralogy* **2012**, *24*, 405–428.
- (35) Kasian, N.; Tuel, A.; Verheyen, E.; Kirschhock, C. E. A.; Taulelle, F.; Martens, J. A. NMR Evidence for Specific Germanium Siting in IM-12 Zeolite. *Chem. Mater.* **2014**, *26*, 5556–5565.
- (36) Odoh, S. O.; Deem, M. W.; Gagliardi, L. Preferential Location of Germanium in the UTL and IPC-2a Zeolites. *J. Phys. Chem. C* **2014**, *118*, 26939–26946.
- (37) Sastre, G.; Pulido, A.; Corma, A. An attempt to predict and rationalize relative stabilities and preferential germanium location in Si/Ge zeolites. *Microporous Mesoporous Mater.* **2005**, *82*, 159–163.
- (38) Shvets, O. V.; Kasian, N.; Zukał, A.; Pinkas, J.; Čejka, J. The Role of Template Structure and Synergism between Inorganic and Organic Structure Directing Agents in the Synthesis of UTL Zeolite. *Chem. Mater.* **2010**, *22*, 3482–3495.
- (39) Shvets, O. V.; Zukał, A.; Kasian, N.; Žilková, N.; Čejka, J. The Role of Crystallization Parameters for the Synthesis of Germanosilicate with UTL Topology, Chemistry – A. *European Journal* **2008**, *14*, 10134–10140.
- (40) Zhang, J.; Yue, Q.; Mazur, M.; Opanasenko, M.; Shamzhy, M. V.; Čejka, J. Selective Recovery and Recycling of Germanium for the Design of Sustainable Zeolite Catalysts. *ACS Sustainable Chem. Eng.* **2020**, *8*, 8235–8246.
- (41) Villaescusa, L. A.; Barrett, P. A.; Kalwei, M.; Koller, H.; Cambor, M. A. Synthesis and Physicochemical Characterization of an Aluminosilicate Zeolite with IFR Topology, Prepared by the Fluoride Route. *Chem. Mater.* **2001**, *13*, 2332–2341.
- (42) Košová, G.; Čejka, J. Incorporation of Aluminum and Iron Into the ZSM-12 Zeolite: Synthesis and Characterization of Acid Sites. *Collect. Czech. Chem. Commun.* **2002**, *67*, 1760–1778.
- (43) Schunk, S. A.; Demuth, D. G.; Schulz-Dobrick, B.; Unger, K. K.; Schüth, F. Element distribution and growth mechanism of large SAPO-5 crystals. *Microporous Materials* **1996**, *6*, 273–285.
- (44) Zhai, M.; Ding, H.; Zeng, S.; Jiang, J.; Xu, S.; Li, X.; Zhu, K.; Zhou, X. Aluminous ZSM-48 Zeolite Synthesis Using a Hydro-isomerization Intermediate Mimicking Allyltrimethylammonium Chloride as a Structure-Directing Agent. *Ind. Eng. Chem. Res.* **2020**, *59*, 11139–11148.
- (45) Ogorzaly, K.; Jajko, G.; Wolski, K.; Zapotoczny, S.; Kubu^o, M.; Roth, W. J.; Gil, B.; Makowski, W. Catalytic activity enhancement in pillared zeolites produced from exfoliated MWW monolayers in solution. *Catal. Today* **2022**, *390–391*, 272–280.
- (46) Kikhtyanin, O.; Chlubná, P.; Jindrová, T.; Kubička, D. Peculiar behavior of MWW materials in aldol condensation of furfural and acetone. *Dalton Transactions* **2014**, *43*, 10628–10641.
- (47) Xing, E.; Shi, Y.; Xie, W.; Zhang, F.; Mu, X.; Shu, X. Temperature-controlled phase-transfer hydrothermal synthesis of MWW zeolites and their alkylation performances. *RSC Adv.* **2016**, *6*, 29707–29717.
- (48) Qin, F.; Wang, Y.; Lu, Y.; Osuga, R.; Gies, H.; Kondo, J. N.; Yokoi, T. Synthesis of novel aluminoborosilicate isomorphous to zeolite TUN and its acidic and catalytic properties. *Microporous Mesoporous Mater.* **2021**, *323*, No. 111237.
- (49) Yang, Y.; Ding, J.; Xu, C.; Zhu, W.; Wu, P. An insight into crystal morphology-dependent catalytic properties of MOR-type titanosilicate in liquid-phase selective oxidation. *J. Catal.* **2015**, *325*, 101–110.
- (50) Roth, W. J.; Dorset, D. L. Expanded view of zeolite structures and their variability based on layered nature of 3-D frameworks. *Microporous Mesoporous Mater.* **2011**, *142*, 32–36.
- (51) Roth, W. J.; Čejka, J.; Millini, R.; Montanari, E.; Gil, B.; Kubu, M. Swelling and Interlayer Chemistry of Layered MWW Zeolites MCM-22 and MCM-56 with High Al Content. *Chem. Mater.* **2015**, *27*, 4620–4629.
- (52) Corma, A.; Rey, F.; Valencia, S.; Jorda, J. L.; Rius, J. A zeolite with interconnected 8-, 10- and 12-ring pores and its unique catalytic selectivity. *Nat. Mater.* **2003**, *2*, 493–497.
- (53) Yuan, R.; Claes, N.; Verheyen, E.; Tuel, A.; Bals, S.; Breynaert, E.; Martens, J. A.; Kirschhock, C. E. A. Synthesis of an IWW-type germanosilicate zeolite using 5-azonia-spiro[4,4]nonane as a structure directing agent. *New J. Chem.* **2016**, *40*, 4319–4324.